

Research Article

Nonlinear in-plane response of 3D-printed concrete walls with varied infill patterns: Experimental mix design and numerical structural assessment

İsmail Hakkı Tarhan ^{a,*} 📵, Yeşim Tarhan ^b 📵

ABSTRACT

This study investigates the nonlinear in-plane structural behavior of 3D-printed concrete wall elements with two representative internal infill patterns – lattice (L) and triangular (T) - using finite element modeling informed by experimentally derived material properties. A printable concrete mixture was specifically developed using CEM I 42.5 R Portland cement, silica sand, and hydroxypropyl methylcellulose (HPMC) as a viscosity-modifying agent. Conventional cast specimens (40×40×160 mm³) achieved a 28-day flexural strength of 8.7 MPa and a compressive strength of approximately 63 MPa. Nonlinear behavior of wall panels with both infill types was investigated using numerical methods with advanced constitutive laws. These models account for the distinct compressive-tensile response of concrete and damage evolution under monotonic lateral loading, allowing assessment of the influence of geometry on load-bearing capacity and failure mechanisms. The results reveal that both infill patterns exhibit nonlinear load-displacement responses with an initial elastic regime, an early localized cracking peak, followed by a notable recovery in load-bearing capacity, and subsequently a global peak load prior to progressive postpeak softening. While the overall performance of both infill types was comparable, the T pattern exhibited a marginally higher peak load (1.7-2.7%) and improved ductility relative to the L form. These distinctions are attributed to the T-pattern's more efficient diagonal force transfer and the development of a single continuous diagonal shear band, as opposed to the L-pattern's multiple discontinuous cracks and broader damage zones.

ARTICLE INFO

Article history:

Received – July 21, 2025 Revision requested – August 20, 2025 Revision received – August 28, 2025 Accepted – September 3, 2025

Keywords:

3D concrete printing In-plane behavior Nonlinear analysis Structural wall members Infill geometry Failure mechanism



This is an open access article distributed under the CC BY licence.
© 2025 by the Authors.

Citation: Tarhan İH, Tarhan Y (2025). Nonlinear in-plane response of 3D-printed concrete walls with varied infill patterns: Experimental mix design and numerical structural assessment. Challenge Journal of Structural Mechanics, 11(3), 160–173.

1. Introduction

Three-dimensional printing (3DP) technology, also known as additive manufacturing, is rapidly transforming the construction industry by enabling complex, customized components to be fabricated directly from digital models - eliminating conventional formwork, streamlining construction, and reducing material waste (Labonnote et al. 2016; Maskuriy et al. 2019; Scheurer et al.

2020; Tarhan et al. 2024a; Mohamed and Mohamed 2025). Notable projects include Dubai's "Office of the Future" – the world's first fully functional 3D-printed office (Fig. 1(a,b)) – printed on site in just 17 days, achieving nearly 50% reductions in labor and material costs (Archdaily 2019; Hossain et al. 2020). In China, WinSun Company demonstrated the speed and efficiency of 3D construction by producing ten single-story homes in Suzhou within 24 hours (Fig. 1(c)). The company also con-

^a Department of Civil Engineering, Tokat Gaziosmanpaşa University, 60150 Tokat, Türkiye

^b Technical Sciences Vocational School, Ardahan University, 75000 Ardahan, Türkiye

^{*} Corresponding author. Tel.: +90-356-252-1616; E-mail address: ismailhakki.tarhan@gop.edu.tr (İ. H. Tarhan) ISSN: 2149-8024 / DOI: https://doi.org/10.20528/cjsmec.2025.03.005

structed a five-story apartment building (Fig. 1(d)) and a 1,100 m² villa using 3D-printed concrete components (Fig. 1(e)). These projects achieved 30–60% reductions

in material waste and up to 70% shorter build times compared to traditional methods (Winsun3d 2015; Zoey 2018; Hossain et al. 2020).



Fig. 1. Examples of large-scale 3D-printed concrete construction: (a),(b) Dubai "Office of the Future" printed by Apis Cor (Archdaily 2019); (c) Single-story houses by WinSun (Architectsjournal 2014); (d) WinSun's five-story apartment building (Winsun3d 2015); (e) Interior corridor of a 3D-printed villa (Zoey 2018).

In addition to these widely recognized benefits, 3D printing allows for the precise replication of historic or ornamental components, as seen by a recent review study (Tarhan and Tarhan 2025). The unique nature of additive manufacturing also opens the door to further possibilities. For instance, the technology may facilitate the seamless integration of multi-functional features, such as embedded sensors or service conduits, directly during fabrication. Its flexibility enables on-demand construction in remote or disaster-affected regions. Furthermore, the ability to locally tailor material composition and geometry presents opportunities for functionally graded elements and resource-efficient, performance-based design. While many of these possibilities remain aspirational in current practice, they represent promising directions for future research and innovation in digital construction.

Despite significant progress in the development of 3D-printable cement-based mixtures with suitable rheological and mechanical properties (Perrot et al. 2016; Rahman et al. 2024; Tarhan et al. 2024b; Zafar et al. 2025), the widespread use of 3D-printed concrete in structural construction is still hindered by several unresolved challenges at the building scale. One of the major

limitations in layer-by-layer fabrication is the challenge of effectively integrating reinforcement into the printed matrix (Bos et al. 2016; Panda et al. 2018). Traditional steel rebars and meshes are difficult to position continuously, prompting research into alternatives such as robotic bar placement synchronized with the print head (Mechtcherine et al. 2021; Nan et al. 2025), interlayer meshes for enhanced crack control (Ramesh et al. 2024; Tarhan et al. 2024b), direct fiber incorporation (steel, glass, polymer) (Christ et al. 2015; Hambach et al. 2019; Le et al. 2012), and even natural fibers like jute for sustainable earth-based mixes (Tarhan et al. 2024b, 2025a), are being explored, suggesting that natural fibers may also enhance ductility and sustainability in cementitious 3D-printed mixtures. Although promising, each strategy presents its own integration and performance challenges - especially when considered alongside the unique properties and behaviors introduced by additive manufacturing.

Another critical and often overlooked issue is the role of internal infill geometry in the structural performance of 3D-printed elements. Unlike conventional cast concrete, 3D-printed components exhibit pronounced anisotropy, interfacial weaknesses between layers, and a

strong dependency on the specific infill pattern employed (Dey et al. 2023; Panda et al. 2018; Wangler et al. 2016; Yang et al. 2023).

Recent research addressing infill pattern of 3D-printed concrete structural elements can be systematically classified into four main categories based on the loading conditions and performance criteria addressed: (i) fire and thermal performance (AlZahrani et al. 2022; Chamatete and Yalçınkaya 2024; Dziura et al. 2023; Hanifa et al. 2025; Suphunsaeng et al. 2025), (ii) axial compressive performance (Han et al. 2022; Khanverdi and Das 2025; Kumar et al. 2025; Zhang et al. 2025a, 2025b), (iii) out-of-plane structural behavior (Aghajani Delavar et al. 2024; Dey et al. 2023; Hernández Vargas et al. 2024) and (iv) in-plane structural behavior (Aghajani Delavar et al. 2024; Warsi et al. 2025a, 2025b).

Regarding fire and thermal performance, recent studies primarily address the optimization of infill geometries in 3D-printed walls for enhanced insulation. Hanifa et al. (2025) experimentally demonstrated that optimized earthen wall segments featuring carefully designed "infinite" cavity patterns achieved a high thermal resistance (R-value $\approx 1.194 \text{ m}^2 \cdot \text{K/W}$) while maintaining structural compressive strength above 4 MPa. Similarly, Dziura et al. (2023) experimentally validated that cellular concrete walls incorporating PUR-foam cavity infills significantly improved thermal insulation performance, achieving a U-value as low as 0.183 W/m²·K, thus meeting stringent Polish building codes without requiring additional insulation layers. Chamatete and Yalçınkaya (2024) numerically showed that lattice infills combined with granular insulation materials (Expanded Polystyrene (EPS) beads, perlite) reduced thermal transmittance by approximately 26-44%; however, efficiency was highly sensitive to filament width, web length, and thermal bridging at shell connections. AlZahrani et al. (2022) numerically optimized multiple infill geometries (square, triangular, hexagonal, rectangular, diamond), revealing that carefully selected shapes significantly lowered effective thermal conductivities (0.122-0.170 W/m·K) compared to conventional masonry and translated into tangible energy savings. Lastly, Suphunsaeng et al. (2025) performed full-scale fire resistance tests on printed concrete walls with varying cavity arrangements, concluding thicker walls with solid concrete infill filaments had superior insulation ratings under a 3-hour ISO-834 fire exposure, and provided validated numerical models to inform design charts linking wall thickness and cavity geometry to thermal performance.

Recent axial compressive behavior studies on 3D-printed walls have highlighted key influences of reinforcement, openings, and infill geometry on structural performance. Han et al. (2022) experimentally tested full-scale printed walls incorporating internal W-shaped truss infill and horizontal steel reinforcement, reporting an unexpected 25% strength reduction due to the reinforcement layers acting as weak planes; they proposed an analytical model to accurately predict axial capacity. Khanverdi and Das (2025) examined the axial performance of full-scale printed walls with vertical reinforcement and a large window opening, showing vertical rebars enhanced ultimate load by 14–26%, tripled energy

absorption, and shifted failure modes from brittle vertical cracking toward localized crushing, whereas openings modestly reduced capacity (~20%). Kumar et al. (2025) conducted a detailed numerical investigation on the axial compressive (vertical in-plane) response of 3Dprinted concrete walls with different internal lattice geometries, using a coupled Concrete Damaged Plasticity and cohesive-zone modeling framework. To systematically assess the role of internal geometry, they adopted the L-, T-, and LT-type infill patterns originally optimized by Dey et al. (2023) for out-of-plane flexural performance, and applied them under pure axial compression. Their results demonstrated that increasing compressive strength shifts damage from filaments to interfaces, while higher interface shear strength delays instability; among the geometries, larger filament-wall contact (Ltype) enhanced load capacity and delayed cracking. Zhang et al. (2025b) explored the influence of filamentcontact patterns in 2-D infill geometries, revealing that rectangular infills with material overlaps retained stiffness and strength, while honeycomb patterns (pointcontact between layers) experienced up to 45% strength loss due to premature vertical-layer buckling.

The studies on out-of-plane (flexural) performance of 3D-printed concrete have highlighted the significant influence of infill topology and optimized geometry on structural efficiency. Hernández Vargas et al. (2024) introduced a stress-driven internal topology optimization method, locally adjusting the filament width within concrete beams (700×100×100 mm) according to calculated stress distributions. Their approach was experimentally validated via three-point bending tests, clearly demonstrating a 47-63% higher flexural strength-to-weight ratio compared to beams produced using a conventional uniform (zig-zag) infill pattern, highlighting geometryguided thickness variation as a viable strategy to enhance structural capacity and reduce material use simultaneously. Similarly, Dey et al. (2023) experimentally evaluated the flexural behavior of four concrete beams (890 mm length) printed with different lattice-based infills (lattice, triangular, lattice-triangular, and sinusoidal), subjected separately to vertical and transverse three-point bending tests. Their experimental and numerical investigations indicated that triangular infills provided the highest transverse flexural strength (~11.5 kN) and about 30% greater stiffness compared to lattice infills, while subsequent numerical optimization identified a 25% horizontal-to-triangular web-length ratio as optimal for maximizing strength-to-weight efficiency. Finally, addressing specifically wall-scale structures, Delavar et al. (2022) analytically and numerically investigated the outof-plane flexural capacity of slender 3D-printed walls, developing closed-form design equations validated against nonlinear finite-element shell-beam models of four wall prototypes. Their results showed that infill layout directly governed whether failure occurred through oneway or two-way bending mechanisms,

Lastly, in-plane (lateral) structural behavior - crucial for seismic performance - has only recently begun to attract focused research on shear strength, energy dissipation, and seismic resilience. Delavar et al. (2024) analytically and numerically investigated reinforced concrete-

framed 3D-printed walls under quasi-static lateral loading, concluding that the presence of infill patterns increases lateral strength mainly due to an increased cross-sectional area, while the specific type of infill pattern had only a limited impact on overall lateral strength. Warsi et al. (2025b) developed a finite-element composite micro-model combining Concrete Damaged Plasticity (CDP) and cohesive-zone modeling for interlayer interfaces, demonstrating that reducing wall height-towidth ratios, integrating edge columns, and providing continuous reinforcement significantly enhanced lateral strength (~30%), stiffness, and energy dissipation. Additionally, Warsi et al. (2025a) numerically assessed earthquake-resistant design methodologies for hollow 3Dprinted walls based on ACI 318-19 and Eurocode 8 provisions, showing that double-layer reinforcement improved lateral load capacity by approximately 31%, ductility (μ =4.36 versus 4.01), and strain distributions compared to single-layer reinforcement layouts, emphasizing the critical interaction between reinforcement arrangement and internal infill geometry for optimized seismic performance.

Collectively, these studies highlight that internal infill topology, interlayer interface quality, and reinforcement detailing significantly influence the nonlinear behavior and seismic capacity of 3D-printed concrete walls; however, to the best of the authors' knowledge, the nonlinear in-plane performance of unreinforced 3D-printed concrete walls with different infill patterns remains entirely unexplored, leaving a major gap in understanding their failure evolution and ultimate lateral resistance.

To address this gap, the present study systematically evaluates the nonlinear in-plane response of unreinforced 3D-printed concrete walls incorporating different infill geometries - named as lattice (L) and triangular (T). Infill forms previously introduced and geometrically optimized by Dey et al. (2023) for out-of-plane flexural behavior - and subsequently employed by Kumar et al. (2025) for axial compression analysis - are adopted here to systematically investigate their effects under in-plane lateral loading, enabling direct comparison across different structural scenarios. A high-performance, 3D-printable cementitious mix was specifically developed and experimentally characterized, and its measured properties directly informed the nonlinear finite element models.

Thus, the current investigation uniquely addresses this research gap, examining how infill patterns impact the overall nonlinear response, stiffness degradation, damage evolution, and ultimate capacity of structural 3D-printed concrete walls under in-plane lateral loading condition. The findings provide the first comparative insights into the role of complex internal geometry on the in-plane structural behavior of unreinforced 3D-printed walls – delivering essential knowledge for the development of next-generation, high-performance digital construction systems.

2. Materials and Methods

This section details the development and characterization of a high-performance, 3D-printable cementitious mixture tailored for digital construction applications. The experimental program includes the optimization of mix composition, followed by a comprehensive assessment of its fresh and hardened mechanical properties. These experimentally determined parameters form the basis for subsequent nonlinear finite element simulations, enabling a realistic evaluation of wall-scale structural performance. The adopted numerical modeling strategy, implemented in Abaqus, utilizes the Mohr-Coulomb failure criterion and explicitly accounts for the distinct tensile and compressive behavior of concrete. The specific infill patterns, selection rationale, and geometric configurations of the wall models are also described in detail.

2.1. Development of 3D-printable cementitious mix

The cement-based mixture used for 3D printing in this study was developed to offer extrudability and good mechanical performance. The materials and mixture details are presented in Tarhan et al. (2025b). It consisted of CEM I 42.5 R Portland cement, ground granulated blast furnace slag (GGBS), plaster (TRADICAL-PF-80 branded), metakaolin clay, fine quartz sand (0–2 mm), water, a polycarboxylate ether-based superplasticizer (SP) and hydroxypropyl methylcellulose (HPMC) as a viscosity-modifying agent. The proportions for 1 m³ of the mixture are presented in Table 1.

Table 1. Mix proportions of the printable concrete.

| Materials | CEM I 42.5 R Portland cement | GGBS | Plaster | Metakaolin clay | Sand 0–0.5 mm | Sand 0.5–2 mm | Water | SP | НРМС | Air content |
|-------------|---------------------------------|------|---------|--------------------|------------------|------------------|-------|-----|------|----------------|
| Amount (kg) | 300 | 100 | 100 | 25 | 535.8 | 831.2 | 200 | 7.5 | 0.6 | %1 |

The cement-based mixture was prepared by mixing all the dry ingredients, including cement, aggregate, GGBS, gypsum, clay and methyl cellulose, together at low speed for one minute. Water was then added in two stages, with the plasticiser mixed into the second portion. Mixing continued for a further two minutes. After a short rest period, the mixture was mixed at high speed for a further two minutes, bringing the total mix-

ing time to approximately six minutes. Continuous mixing was used to minimise the risk of premature setting. Penetration depth tests were initially performed to assess printability, but the final mixture was selected based on actual 3D printing trials to ensure suitability. Prismatic samples measuring $40\times40\times160$ mm were cast in molds for flexural and compressive strength testing. After curing for one day under ambient laboratory

conditions, the specimens were demolded and placed in a controlled curing chamber at 20±3 °C with 80% relative humidity until the day of testing, following the approach adopted also in Tarhan et al. (2024b). Meanwhile, 3D-printed samples measuring 110×110×350 mm were fabricated to demonstrate the printability of

the developed mix in terms of its rheological performance.

The 3D printing process was carried out using a Delta WASP 3DMT printer with a 3 cm nozzle operating at a speed of 2 cm/s. Fig. 2 shows the 3D printing process and representative views of the printed layers.



Fig. 2. 3D printing of test samples using a Delta WASP 3DMT printer:
(a) Extrusion of successive layers during printing; (b) Side view of the printed layers with height measurement; (c) Top view of the printed layers with width measurement.

2.2. Experimental characterization of printable concrete

The printable mixture was formulated to ensure adequate buildability and extrusion stability, taking into account the specific rheological demands of layer-by-layer deposition. Key fresh-state parameters were assessed immediately after mixing in order to capture the time-dependent behavior of the material.

The properties of the cement-based mortar in its fresh state were evaluated through a series of standardized tests. Density was measured according to BS EN 12350-6 (2019) and rheological behavior was assessed using a rotational rheometer with four-blade vane geometry. A constant shear rate of $0.05~\rm s^{-1}$ was applied for 200 seconds and the peak torque at flow onset was used to determine the static yield stress, which affects the material's printability and ability to retain its shape. To mon-

itor structuration over time, rheological measurements were repeated at defined intervals. Additionally, the structural build-up was examined using the fall cone penetration method in accordance with CEN ISO 17892-6:2017. The penetration depth of an 80 g, 30° cone dropped into fresh mortar served as an indicator of evolving shear resistance and thixotropic behavior. These combined tests provided insight into the time-dependent characteristics of the mixture, which are critical for ensuring adequate buildability and interlayer adhesion in 3D printing applications.

For material characterization, mold-cast prism specimens were evaluated for mechanical testing. Flexural strength was determined via three-point bending tests on prism specimens with nominal dimensions of $40\times40\times160$ mm, in accordance with TS EN 12390-5 (2019). Following test, the broken halves were tested for compressive strength in accordance with TS EN 12390-3 (2019).

2.3. Numerical modeling approach

The in-plane structural performance of the 3D-printed concrete walls was assessed using nonlinear finite element simulations performed in Abaqus (Abaqus 2022). A macro modeling strategy was adopted, wherein the layered filament architecture of the walls was treated as a homogenized continuum. All solid regions, including the outer wall regions and infill forms, were discretized using four-node linear tetrahedral elements (C3D4). This element type was selected for its suitability with complex geometries, effectiveness in capturing the localized cracking and post-peak softening typical of brittle materials, while maintaining computational efficiency.

The material nonlinearity was represented by the CDP model, which is well established for simulating the inelastic behavior of concrete and similar quasi-brittle materials (Sümer and Aktaş 2015). The CDP model integrates the effects of tensile cracking and compressive crushing by combining plasticity with progressive damage mechanics. The deviatoric yield surface is defined by K_c =2/3, which corresponds to the Mohr–Coulomb criterion in the deviatoric plane (Fig. 3).

Distinct tensile and compressive responses are defined through separate stress–strain relationships for each loading mode. The progressive accumulation of microcracks under tension and crushing damage under compression is tracked using two independent scalar damage variables, d_t and d_c , which reduce the material's elastic modulus with increasing strain, thereby realisti-

cally capturing stiffness degradation. In tension, the model captures the linear elastic response up to the tensile strength, followed by strain-softening due to crack development. In compression, the response includes an initial linear regime, limited hardening, and subsequent exponential softening after peak stress (Fig. 4).

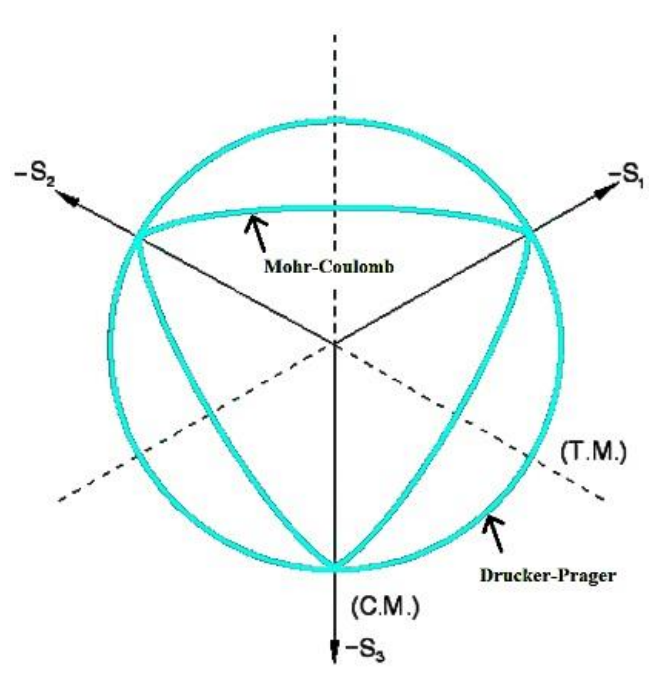


Fig. 3. Deviatoric yield surfaces for Mohr–Coulomb $(K_c=2/3)$ and Drucker–Prager $(K_c=1)$ criteria.

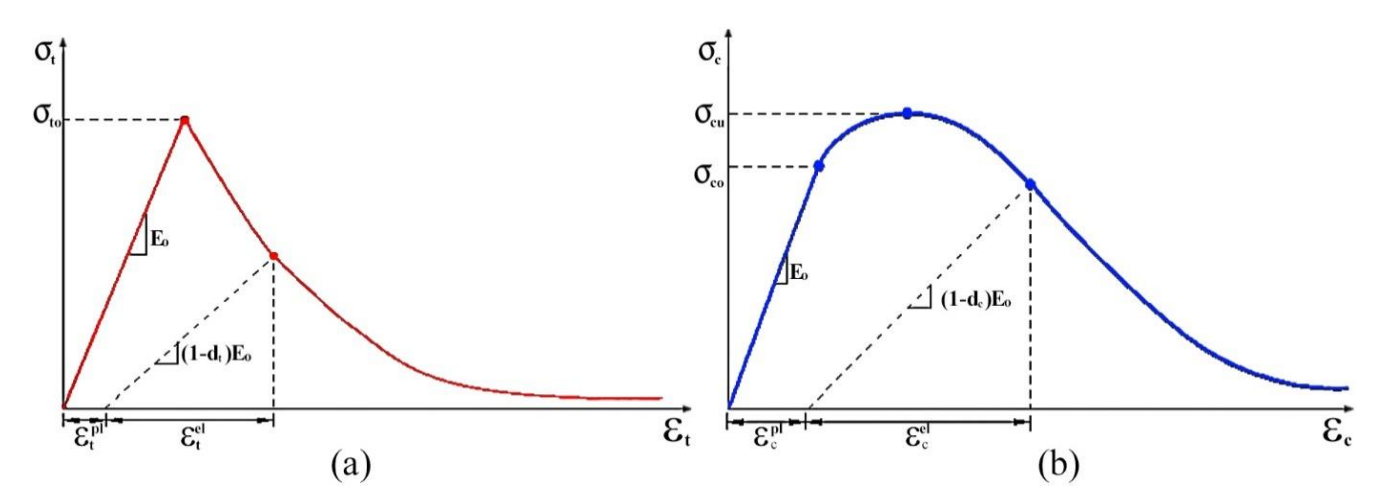


Fig. 4. Material response under (a) tension and (b) compression.

Additional CDP input parameters included a dilation angle of 30°, flow potential eccentricity of 0.1, and a biaxial-to-uniaxial compressive strength ratio of 1.16, reflecting common practice for concrete (Lubliner et al. 1989; Tarhan 2025a). To aid convergence in the postpeak regime, a small viscosity parameter of 0.0001 was introduced, which has negligible effect on the global structural response but improves numerical stability in the softening range (Abaqus 2022; Tarhan 2025b). Material properties (Table 2) and nonlinear constitutive parameters were directly obtained from the experimentally validated cementitious mix, as detailed in Sections

2.1 and 3.1. The direct tensile strength (f_t) of the concrete was estimated as half of the measured flexural strength. The CDP model parameters were implemented as described above, with no further calibration.

2.4. Infill pattern selection, description and wall models

In this study, geometric models of the 3D-printed concrete walls were developed to include both outer wall regions and two distinct internal infill patterns: lattice (L) and triangular (T). These forms were originally intro-

duced and optimized for out-of-plane flexural efficiency by Dey et al. (2023) and later utilized by Kumar et al. (2025) in axial compression studies. By adopting these well-established patterns, the present work contributes complementary insights into their structural performance under in-plane monotonic lateral loading thereby extending the existing knowledge base to encompass a broader range of loading conditions and enabling a more comprehensive understanding of their behavior in digital construction applications (Fig. 5).

| | | | 1 1 | | | |
|---------------|-----------------------|----------------------|-----------------------|----------------------|---------------------|--|
| | | M | Mechanical properties | | | |
| Density (kg/n | 1 ³) Youn | g's modulus (MPa) | Poisson's ratio | f _c (MPa) | $f_t(MPa)$ | |
| 2,150 | 2,150 | | 0.2 | 63 | 4.3 | |
| | | | Plasticity definition | | | |
| Dilation angl | e | Eccentricity | f_{b0}/f_{c0} | K_c | Viscosity parameter | |
| 30° | | 0.1 | 1.16 0.667 | | 0.0001 | |
| | Stress-inelastic | strain relationships | | Damage o | lefinition | |
| Compr | Compressive | | ile | Tension | | |
| Yield stress | Inelastic strain | Yield stress | Cracking strain | Damage parameter | Cracking strain | |
| 20 | 0 | 4.3 | 0 | 0 | 0 | |
| 40 | 0.0012 | 0.43 | 0.003 | 0.9 | 0.003 | |
| 55 | 0.002 | - | - | - | - | |
| 63 | 0.0032 | - | - | - | - | |
| 50 | 0.0075 | - | - | - | - | |
| 31 | 0.012 | _ | - | - | - | |
| 10 | 0.017 | | _ | | _ | |

Table 2. Adopted material properties.

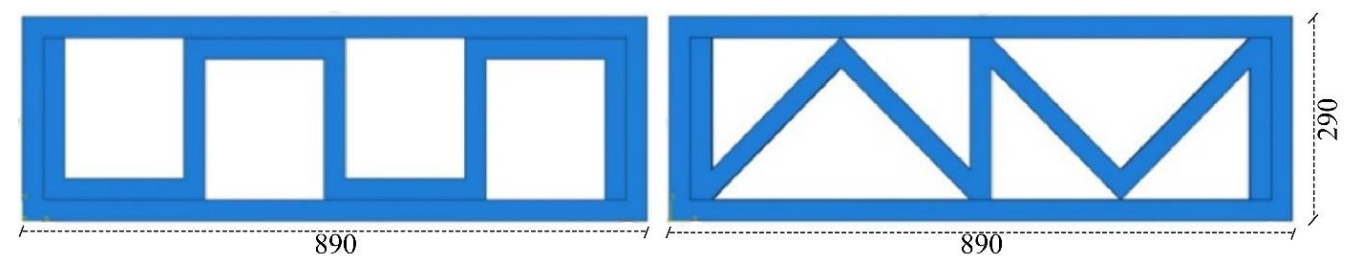


Fig. 5. Schematic representations of the two 3D-printed concrete wall models with different internal infill patterns: (left) L and (right) T adapted from Dey et al (2023) (all dimensions are in millimeters).

All wall geometries were created in SolidWorks and subsequently imported into Abaqus for numerical modeling. Walls were defined with a cross-sectional size of 890 mm×290 mm, consistent with the reference configuration adopted by Dey et al. (2023) (Fig. 5). The layer width and height were 30 and 20 mm, respectively, reflecting the printing process of the experimentally produced mix and ensuring compatibility with common extrusion-based 3D printing processes. An aspect ratio (height to width) of approximately 1:0.5 was adopted, resulting in a total of 85 layers per wall (Fig. 6) - matching the practical constraints and design parameters addressed in Sections 2.1 and 2.2.

According to the adopted macro modeling approach, all interfaces between deposited filaments within a layer, as well as between successive layers, were inherently assumed fully bonded. This means that potential interlayer weaknesses were not explicitly modeled in this study. Such simplification reflects both the cohesive quality ob-

served in the developed 3D-printable mix and prevailing practice in comparable numerical studies. By excluding interface imperfections, the numerical model isolates the structural influence of infill geometry, thereby establishing a benchmark for future studies where interlayer bonding effects may be directly incorporated.

Finite element meshes were generated using four-node linear tetrahedral elements (C3D4), which enabled accurate representation of the complex internal geometries of the wall models (see Fig. 7 for mesh illustration). To assess the influence of mesh dependency on the simulation results, two different mesh densities were employed: a fine mesh with an average element size of 15 mm and a medium mesh of 30 mm. The L-wall models contained 28801 nodes and 126464 elements with the medium mesh and 91481 nodes and 458348 elements with the fine mesh, while the T-wall models contained 35480 and 73567 nodes with 114272 and 280877 elements, respectively.

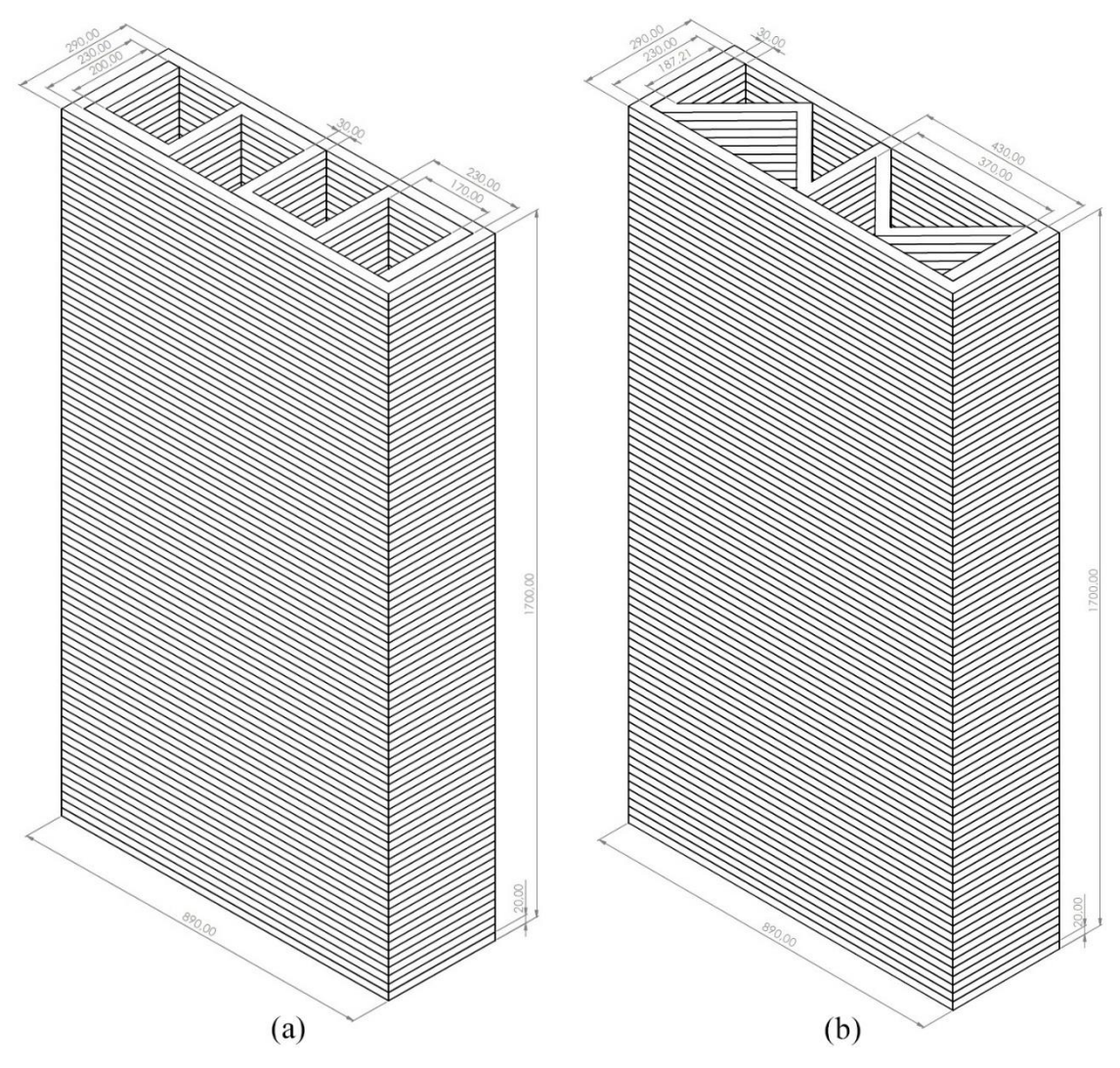


Fig. 6. Three-dimensional CAD views of the 3D-printed wall panels with (a) L and (b) T internal infill patterns (all dimensions are in millimeters).

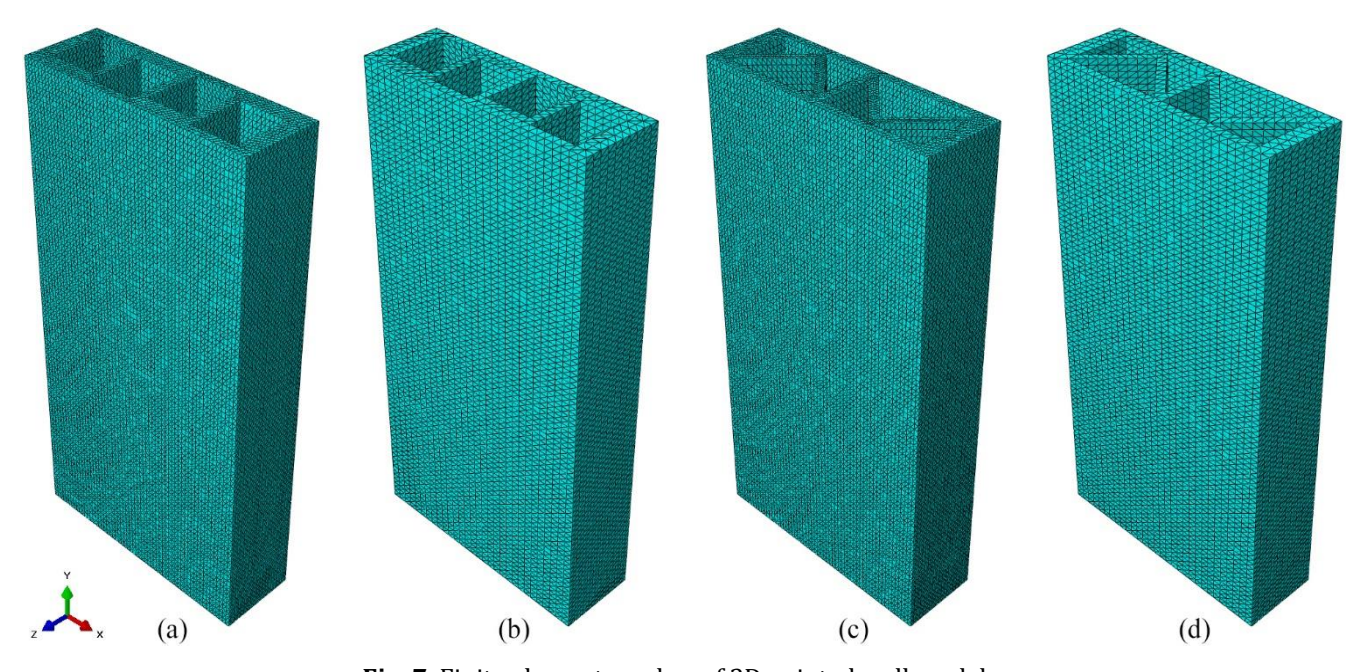


Fig. 7. Finite element meshes of 3D-printed wall models: (a,b) L pattern with fine and medium mesh densities; (c,d) T pattern with fine and medium mesh densities. All meshes are created using four-node linear tetrahedral elements (C3D4).

In the initial step, boundary conditions were defined: the bottom surface of each wall - including both outer wall regions and infill - was fully fixed (encastre) to represent a rigid foundation, restraining all translational and rotational degrees of freedom. At the top edge, all rotational degrees of freedom and translation in the out-ofplane direction (*Z*) were restricted, while horizontal translation in the loading direction (X, in-plane) and vertical translation (Y, wall height) were left free to allow realistic deformation during loading. Numerical simulations were performed in three consecutive analysis steps to capture realistic loading conditions. First, gravity loading was applied to each wall to account for selfweight. In the second step, an additional vertical precompressive load - equal to the calculated self-weight of the wall (4,350 N for the T-pattern, 4,378 N for the L-pattern, based on a measured density of 2.15 g/cm³) - was applied uniformly over the top surface. This step simulated the scenario where the wall supports another identical story above. In the final step, a monotonic lateral displacement was incrementally imposed at the top surfaces until global failure was reached.

3. Results and Discussion

3.1. Fresh and hardened properties of concrete

At the beginning of the testing process, the cement-based mortar had a unit weight of $2.15~\rm g/cm^3$, which indicates that it is a dense, well-compacted mixture that is suitable for structural applications. The penetration depth measured by the fall cone test was $19.74~\rm mm$, reflecting a moderate level of thixotropy and structural build-up in the early stages. Rheological characterization using a rotational rheometer yielded a peak torque of $9.4~\rm mNm$ at a shear rate of $0.05~\rm s^{-1}$, corresponding to the static yield stress of the mix. These values confirm that the mortar possesses adequate resistance to deformation while maintaining sufficient flowability for extrusion-based 3D printing.

The cement-based printable mortar exhibited rapid strength development, with compressive strength in-

creasing from 10.96 MPa at 1 day to 53.75 MPa by day 14 and reaching 62.89 MPa at 28 days. This places the mix in the TS EN 206+A2 (2021) strength class C50/60, indicating its classification as a high-performance mortar. Such rapid hardening is typical of low water-to-binder ratio mixtures with reactive fillers and ensures early load-bearing capacity for successive layers. Flexural strength rose from 3.93 MPa at 1 day to 8.70 MPa at 28 days, demonstrating adequate tensile resistance comparable to engineered 3D-printed mortars reported in the literature.

3.2. Nonlinear in-plane behavior of 3D printed concrete walls

This section presents the nonlinear in-plane response of 3D-printed concrete wall models incorporating L and T infill patterns. Finite element analyses were performed with two mesh densities (fine and medium) to assess mesh sensitivity and the robustness of the results. Fig. 8 shows the load–displacement curves obtained for each configuration, and numerical data are summarized in Table 3.

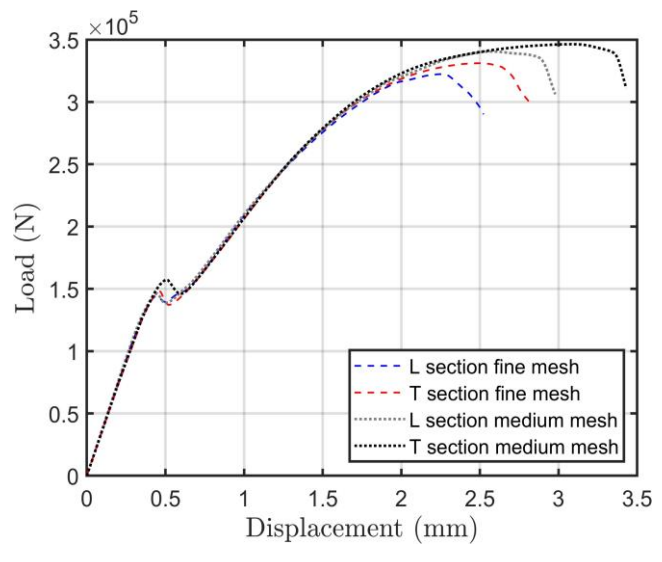


Fig. 8. Load–displacement curves of L and T-pattern wall models, showing higher peak load and ductility for the T-pattern across both mesh densities.

Table 3. Key performance metrics of 3D-printed wall models, including damage initiation and peak load values for each mesh and infill configuration.

| Model | Displacement at damage initiation (mm) | Load (kN) at damage initiation | Displacement at peak load (mm) | Peak load (kN) | |
|----------|---|-----------------------------------|-----------------------------------|-------------------|--|
| L-fine | 0.45 | 144.5 | 2.24 | 322.3 | |
| T-fine | 0.46 | 148.0 | 2.50 | 331.1 | |
| L-medium | 0.45 | 146.2 | 2.57 | 340.5 | |
| T-medium | 0.50 | 157.2 | 3.08 | 346.3 | |

Under monotonic lateral loading, all wall models exhibited a typical nonlinear load-displacement response characterized by an initial stiff elastic regime, a progressive reduction in stiffness with increasing displacement, and a final softening branch associated with material damage and loss of load-bearing capacity. Both L- and T-patterns displayed qualitatively similar behavior, with

discernible differences in ultimate strength, ductility, and crack evolution.

Notably, all wall models exhibited a local load peak at approximately 0.45–0.5 mm displacement, followed by a sharp drop. This first peak corresponds to the onset of localized cracking, predominantly at the outer wall regions adjacent to infill openings (Figs. 9 and 10).

After this initial damage, the models demonstrated a pronounced recovery in load-bearing capacity – evidenced by the renewed increase in the load-displacement curve – thanks to the redistribution of internal forces through undamaged regions and alternative load-bearing paths retained within the infill geometry. This is a direct result of the cellular infill layouts, where alternative load paths can be mobilized after local failure.

As loading continued, crack propagation and accumulated damage caused further stiffness degradation and post-peak softening, culminating in global failure when the primary load paths were fully fractured and the structure could no longer sustain increasing displacement.

Crack evolution differed significantly between patterns (Fig. 9 for L, Fig. 10 for T). Cracking in the L-pattern

typically initiates as short horizontal cracks at the wall base or at the interface between the infill and the outer wall. As loading progresses, three distinct diagonal damage bands emerge, each associated with a different panel region separated by the two vertical struts of the infill. The central diagonal band may eventually link to one of its neighbors, leaving only two main diagonal planes active. Because these bands do not combine into a single continuous failure plane, damage remains confined to separate regions. When stress tends to concentrate within the infill, local post-peak failure zones emerge – these trigger abrupt load drops and accelerate stiffness degradation. The overall failure mode is characterized by the formation of multiple, discontinuous diagonal cracks rather than a single dominant shear plane.

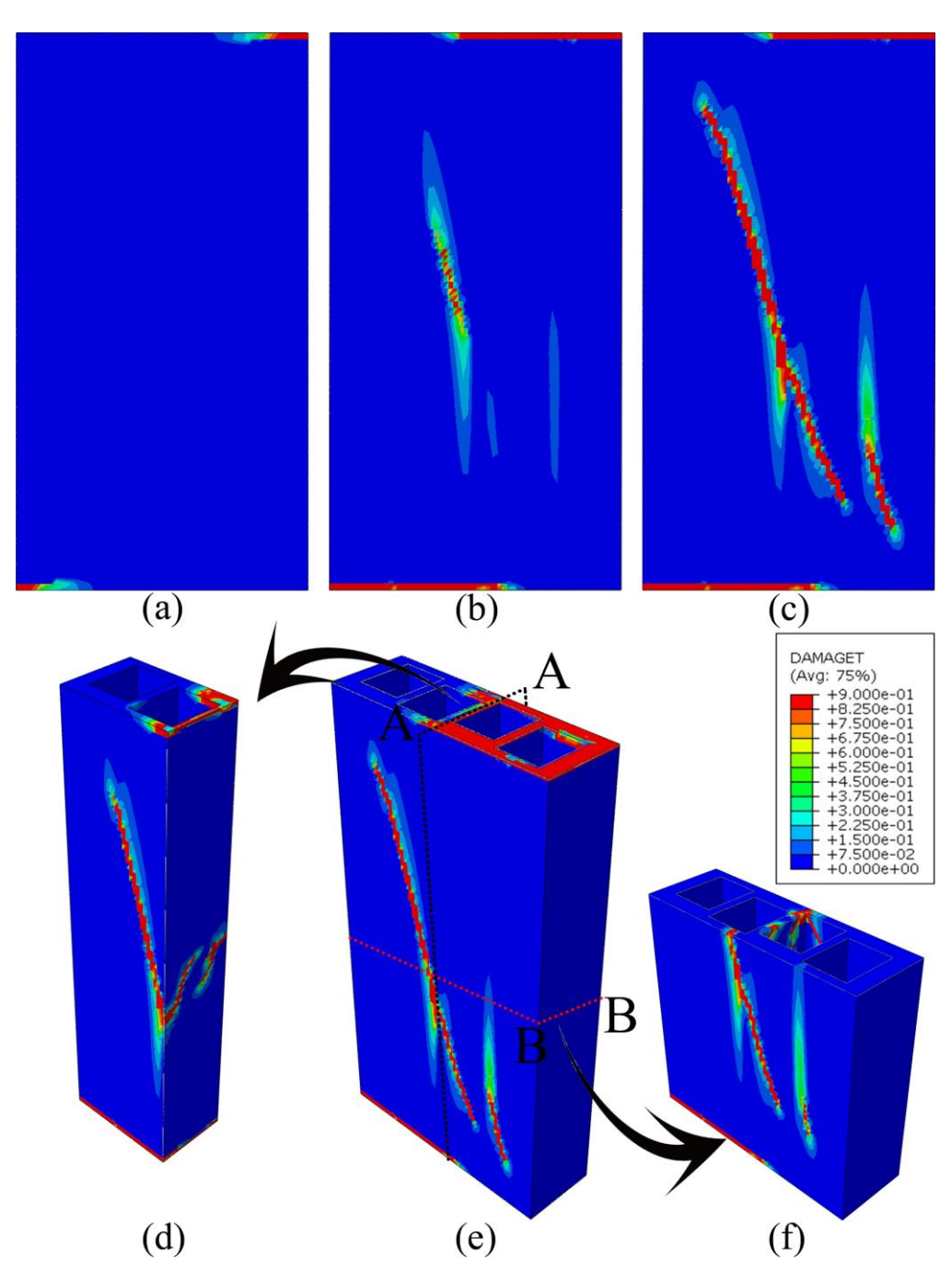


Fig. 9. L-pattern wall: (a–c) Front views of crack initiation and propagation; (d–f) 3D views showing discontinuous diagonal bands and local damage zones.

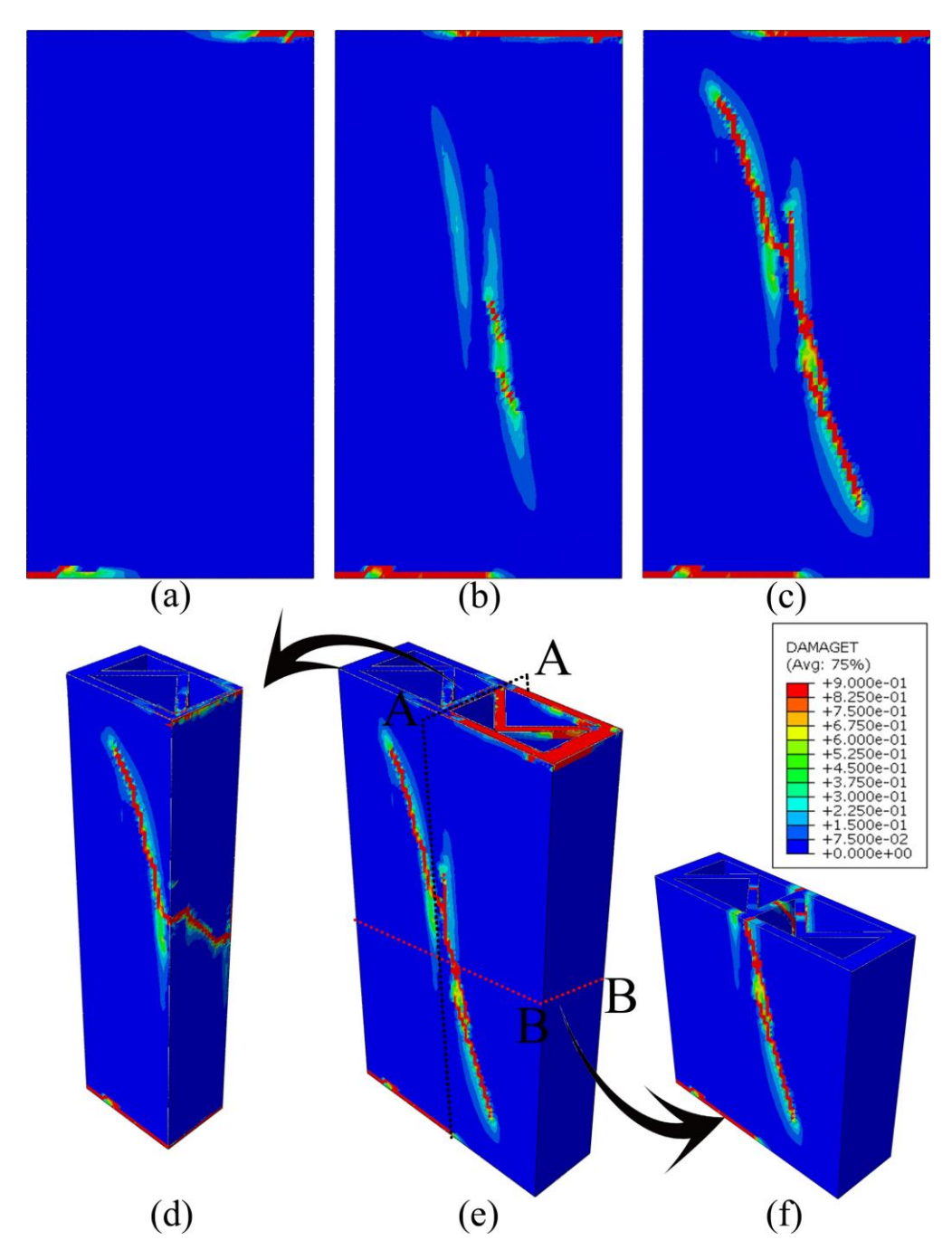


Fig. 10. T-pattern wall: (a–c) Front views of crack initiation and merging; (d–f) 3D views showing a continuous diagonal shear band linking infill and outer wall.

In the T-pattern, initial cracks develop as short horizontal fissures at the base and top of the wall. With further displacement, two separate diagonal cracks form, originating from the bottom corners and propagating upward and inward along the main diagonal load paths of the triangular infill. These cracks eventually merge into a single continuous diagonal damage band, often linking the infill and the outer wall.

For both mesh densities, the T-pattern walls achieved higher peak loads and exhibited modestly higher postpeak ductility compared to the L-pattern walls. Specifically, the T-pattern (medium mesh) reached a maximum load of $\sim\!346$ kN at a displacement of 3.08 mm, while the L-pattern (medium mesh) achieved a lower maximum of $\sim\!340$ kN at a displacement of 2.57 mm. For the fine mesh

models, the T-pattern again showed a higher peak load of \sim 331 kN, compared to the L-pattern at \sim 322 kN. This corresponds to a 1.7–2.7% higher peak load for T-patterns, depending on mesh size. First cracking consistently occurred at \sim 0.45–0.5 mm displacement, with initial crack loads ranging from 144.5 kN (L-fine) to 157.2 kN (T-medium).

Across all models, fine mesh solutions showed marginally earlier softening and slightly reduced post-peak load retention, due to their increased ability to localize damage and capture brittle post-peak behavior. These results confirm that the triangular infill, characterized by continuous diagonal load paths and efficient stress distribution, enhances both the load-bearing capacity and the energy dissipation after peak.

Mesh sensitivity was minimal; peak load deviation was less than 3%, with the fine mesh leading to marginally earlier softening and reduced post-peak load retention due to better localization of damage.

Although the formation of a single continuous diagonal crack in the T-pattern might intuitively seem to promote rapid structural failure, the simulation results demonstrate the opposite: the T-pattern achieves higher peak load and superior post-peak energy dissipation. This advantage is attributable to the geometric efficiency of having only one central strut, which creates two main load-bearing zones and focuses diagonal shear transfer through a direct, robust path. In contrast, the L-pattern's two interior struts divide the wall into three distinct regions, resulting in a broader area of damage and increased stress concentrations at multiple infill junctions. Consequently, the L-pattern exhibits more extensive diagonal cracking, greater localized damage. and slightly reduced capacity. This difference in internal force distribution explains why the T-pattern, despite exhibiting a continuous diagonal crack, outperforms the L-pattern in both strength and ductility. These findings align with the observed crack maps (Fig. 9 for L, Fig. 10 for T), which show multiple discontinuous diagonal cracks in the L-pattern but a more unified damage band in the T-pattern.

In conclusion, the internal geometry decisively influences both the strength and the nature of failure. While both patterns display mixed-mode (flexural and shear) cracking, the T-pattern demonstrates marginally better performance, which can inform infill strategy selection for digitally constructed walls.

4. Conclusions

This study investigated the nonlinear in-plane behavior of 3D-printed concrete walls with two distinct infill geometries-lattice (L) and triangular (T)-using finite element modeling informed by experimentally derived material properties. A printable cementitious mortar, characterized by high early-age strength and shape stability, was specifically developed, and its mechanical characteristics were incorporated into the simulations to ensure realistic representation of structural performance.

Key findings are as follows:

- Both infill types exhibited a distinct nonlinear response under monotonic lateral loading, characterized by an initial elastic regime, a localized load drop associated with crack initiation, a subsequent recovery phase due to internal force redistribution, and progressive post-peak softening as damage accumulated.
- T-pattern demonstrated superior performance, achieving 1.7–2.7% higher peak loads and improved ductility, attributed to its centralized diagonal force path and efficient stress redistribution, as opposed to the multiple discontinuous cracking bands observed in the L-pattern.
- Crack development in the T-walls followed a dominant diagonal shear band linking the outer wall and

- infill, while L-walls exhibited multiple damage zones with broader failure areas due to the division created by the two interior struts.
- Damage consistently initiated at ~0.45-0.50 mm displacement, highlighting critical stress concentrations near infill interfaces. Post-peak deterioration was governed by damage localization in both the outer wall and the infill regions.
- Incorporating fine mesh allowed improved resolution of damage localization and sharper post-peak degradation, though mesh sensitivity remained minimal for global response metrics.

However, interlayer interfaces were not explicitly modeled in the simulations. Although the developed mortar exhibited high cohesion and produced structurally robust printed elements, most printable mixtures may contain interfacial defects or exhibit weak layer bonding due to the nature of the layer-by-layer deposition process. These interfaces can significantly influence crack initiation and propagation. Therefore, future studies should incorporate interface effects (e.g. with cohesive contact definitions) or experimentally calibrated interface models to capture interface-driven damage mechanisms and better reflect the performance variability observed in real printed structures.

Moreover, while the effects of different infill geometries were assessed through two representative patterns, a more comprehensive understanding may be achieved by employing topology optimization algorithms that account for both in-plane and out-of-plane behavior. Such methods could reveal optimal hybrid infill forms tailored for multi-directional performance and material efficiency. In addition, experimental validation at full scale is needed to confirm the damage patterns observed numerically, particularly under cyclic or combined loadings representative of real-world conditions.

Acknowledgements

None declared.

Funding

The authors received no financial support for the research, authorship, and/or publication of this manuscript.

Conflict of Interest

The authors declared no potential conflicts of interest with respect to the research, authorship, and/or publication of this manuscript.

Author Contributions

All of the authors made substantial contributions to conception and design, or acquisition of data, or analysis and interpretation of data; were involved in drafting the manuscript or revising it critically for important intellectual content; and gave final approval of the version to be published.

Data Availahility

The datasets created and/or analyzed during the current study are not publicly available, but are available from the corresponding author upon reasonable request.

REFERENCES

- Aghajani Delavar M, Chen H, Sideris P (2024). Analysis and design of 3D printed reinforced concrete walls under in-plane quasi-static loading. *Engineering Structures*, 303, 117535.
- AlZahrani AA, Alghamdi AA, Basalah AA (2022). Computational optimization of 3D-printed concrete walls for improved building thermal performance. *Buildings*, 12(12), 2267.
- Archdaily (2019). Dubai municipality to become the world's largest 3D-printed building. http://www.archdaily.com/930857/dubai-municipality-to-become-the-worlds-largest-3d-printed-building [accessed 27-08-2025].
- Architectsjournal (2014). Chinese firm prints ten houses in a day. http://www.architectsjournal.co.uk/news/chinese-firm-prints-ten-houses-in-a-day [accessed 27-08-2025].
- Bos F, Wolfs R, Ahmed Z, Salet T (2016). Additive manufacturing of concrete in construction: Potentials and challenges of 3D concrete printing. *Virtual and Physical Prototyping*, 11(3), 209-225.
- BS EN 12350-6 (2019). Testing fresh concrete Part 6: Density. British Standards Institution (BSI), London, UK.
- CEN ISO 17892-6 (2017). Geotechnical investigation and testing Laboratory testing of soil Part 6: Fall cone test. International Organization for Standardization (ISO), Geneva, Switzerland.
- Chamatete K, Yalçınkaya Ç (2024). Numerical evaluation on thermal performance of 3D printed concrete walls: The effects of lattice type, filament width and granular filling material. *Buildings*, 14(4), 926.
- Christ S, Schnabel M, Vorndran E, Groll J, Gbureck U (2015). Fiber reinforcement during 3D printing. *Materials Letters*, 139, 165-168.
- Delavar MA, Chen H, Sideris P (2022). Analytical and numerical investigation of out-of-plane behavior of 3D printed concrete walls. *Proceedings of the 12th National Conference on Earthquake Engineering*, Salt Lake City, Utah, USA.
- Dey D, Van VN, Xuan HN, Srinivas D, Panda B, Tran P (2023). Flexural performance of 3D printed concrete structure with lattice infills. *Developments in the Built Environment*, 16, 100297.
- Dziura P, Maroszek M, Góra M, Rudziewicz M, Pławecka K, Hebda M (2023). Influence of the in-fill pattern of the 3D printed building wall on its thermal insulation. *Materials*, 16(17), 5772.
- Hambach M, Rutzen M, Volkmer D (2019). Properties of 3D-printed fiber-reinforced portland cement paste. In: Sanjayan J, Nazari A, Nematollahi B, editors. 3D Concrete Printing Technology. Elsevier, Amsterdam, Netherlands, 73-113.
- Han X, Yan J, Liu M, Huo L, Li J (2022). Experimental study on largescale 3D printed concrete walls under axial compression. *Automa*tion in Construction, 133, 103993.
- Hanifa MF, Mendonça P, Figueiredo B, Mahdy D (2025). Experimental study on the thermal performance of 3D-printed earthen wall segment with optimized infill pattern. In: Cruz P, editor. *Structures and Architecture*. CRC Press, London, UK, 1692-1699.
- Hernández Vargas J, Sjölander A, Westerlind H, Silfwerbrand J (2024). Internal topology optimisation of 3D printed concrete structures: A method for enhanced performance and material efficiency. *Virtual and Physical Prototyping*, 19(1), e2346290.
- Hossain MA, Zhumabekova A, Paul SC, Kim JR (2020). A review of 3D printing in construction and its impact on the labor market. *Sustainability*, 12(20), 8492.
- Khanverdi M, Das S (2025). Performance of full-scale 3D-printed concrete walls: Effects of vertical reinforcements and window opening. Engineering Structures, 337, 120510.
- Kumar SS, Muthu N, Panda B (2025). Numerical investigation of structural behavior of 3D-printed concrete walls: From damage mechanics to cohesive zone approaches. *Progress in Additive Manufacturing*, In Press.
- Labonnote N, Rønnquist A, Manum B, Rüther P (2016). Additive construction: State-of-the-art, challenges and opportunities. *Automation in Construction*, 72, 347-366.
- Le TT, Austin SA, Lim S, Buswell RA, Law R, Gibb AGF, Thorpe T (2012). Hardened properties of high-performance printing concrete. *Cement and Concrete Research*, 42(3), 558-566.

- Lubliner J, Oliver J, Oller S, Oñate E (1989). A plastic-damage model for concrete. *International Journal of Solids and Structures*, 25, 299-326.
- Maskuriy R, Selamat A, Maresova P, Krejcar O, David OO (2019). Industry 4.0 for the construction industry: Review of management perspective. *Economies*, 7(3), 68.
- Mechtcherine V, Buswell R, Kloft H, Bos FP, Hack N, Wolfs R, Sanjayan J, Nematollahi B, Ivaniuk E, Neef T (2021). Integrating reinforcement in digital fabrication with concrete: A review and classification framework. *Cement and Concrete Composites*, 119, 103964.
- Mohamed RA, Mohamed AFA (2025). Exploring the environmental benefits of 3D printing technology in concrete construction: A review. *Progress in Additive Manufacturing*, 10(1), 279-289.
- Nan B, Qiao Y, Leng J, Bai Y (2025). Advancing structural reinforcement in 3D-printed concrete: Current methods, challenges, and innovations. *Materials*, 18(2), 252.
- Panda B, Unluer C, Tan MJ (2018). Investigation of the rheology and strength of geopolymer mixtures for extrusion-based 3D printing. *Cement and Concrete Composites*, 94, 307-314.
- Perrot A, Rangeard D, Pierre A (2016). Structural built-up of cement-based materials used for 3D-printing extrusion techniques. *Materials and Structures*, 49(4), 1213-1220.
- Rahman M, Rawat S, Yang R, Mahil A, Zhang YX (2024). A comprehensive review on fresh and rheological properties of 3D printable cementitious composites. *Journal of Building Engineering*, 91, 109719.
- Ramesh A, Rajeev P, Sanjayan J, Mechtcherine V (2024). In-process textile reinforcement method for 3D concrete printing and its structural performance. *Engineering Structures*, 314, 118337.
- Scheurer M, Dittel G, Gries T (2020). Potential for the integration of continuous fiber-based reinforcements in digital concrete production. In: Bos FP, Salet T, editors. *3D Printing in Concrete: Materials, Processes and Applications.* Springer, Berlin, Germany, 701-711.
- Suphunsaeng K, Prasittisopin L, Pethrung S, Pansuk W (2025). Fire performance evaluation of 3D-printed concrete walls: A combined full-scale and numerical modeling approach. *Journal of Building Engineering*, 104, 112296.
- Tarhan Y, Tarhan İH, Şahin R (2024a). Comprehensive review of binder matrices in 3D printing construction: Rheological perspectives. *Buildings*, 15(1), 75.
- Tarhan Y, Tarhan İH, Jacquet Y, Perrot A (2024b). Mechanical behaviour of 3D printed and textile-reinforced eco-friendly composites. *Journal of Sustainable Cement-Based Materials*, 14(3), 477–495.
- Tarhan İH, Tarhan Y (2025). Cultural heritage conservation in digital era: A review of digital twin and 3D printing applications. *Uludağ University Journal of the Faculty of Engineering*, In Press.
- Tarhan Y, Tarhan İH, Perrot A (2025a). Improving bond performance of 3D-printable earth-based mortar reinforced with jute fibers. Challenge Journal of Structural Mechanics, 11(2), 99-105.
- Tarhan Y, Tarhan İH, Perrot A (2025b). Flexural performance of glass fibre textile reinforced 3D printed concrete. Proceedings of the 4th International Civil Engineering & Architecture Conference, Trabzon, Türkiye, 1509-1515.
- Tarhan İH (2025a). Nonlinear in-plane behavior of masonry walls strengthened with optimally distributed fiber reinforced polymer. *Engineering Failure Analysis*, 182(Part A), 110035.
- Tarhan İH (2025b). Stepwise FRP strengthening of historical masonry minarets: Nonlinear seismic assessment based on a minaret collapsed during the 2023 Kahramanmaraş earthquakes. *Engineering Failure Analysis*. 180. 109933.
- TS EN 12390-3 (2019). Testing hardened concrete Part 3: Compressive strength of test specimens. Turkish Standards Institute, Ankara, Türkiye.
- TS EN 12390-5 (2019). Testing hardened concrete Part 5: Flexural strength of test specimens. Turkish Standards Institute, Ankara, Türkiye.
- Wangler T, Lloret E, Reiter L, Hack N, Gramazio F, Kohler M, Bernhard M, Dillenburger B, Buchli J, Roussel N, Flatt R (2016). Digital concrete: Opportunities and challenges. RILEM Technical Letters, 1, 67-75.
- Warsi SBF, Panda B, Biswas P (2025a). Design of earthquake-resistant 3D printed concrete wall based on ACI 318–19: Analytical investigation and numerical modelling. *Structures*, 78, 109371.

- Warsi SBF, Panda B, Biswas P (2025b). Structural analysis of 3D-printed concrete walls under quasi-static cyclic loading using composite micro-model. *Progress in Additive Manufacturing*, 10(8), 4901-4921.
- Winsun3d (2015). 2015 global highest 3D printing building. http://www.winsun3d.com/En/Product/pro_inner_5/id/102 [accessed 27-08-2025].
- Sümer Y, Aktaş M (2015). Defining parameters for concrete damage plasticity model. *Challenge Journal of Structural Mechanics*, 1(3), 149-155.
- Zafar MS, Javadnejad F, Hojati M (2025). Optimizing rheological properties of 3D printed cementitious materials via ensemble machine learning. *Additive Manufacturing*, 109, 104889.
- Zhang B, Tao Y, Zhang Y, Shields Y, De Corte W, Wan-Wendner R (2025a). Mechanical properties of 3D printed concrete with 2D infill patterns including print path crossings. *Construction and Building Materials*, 483, 141764.
- Zhang B, Zhang Y, Ye Y, Hao L, Cui W, Yang H, Tao Y (2025b). Influence of contacts in 2D infill patterns on mechanical properties of 3D printed concrete structures. *Materials Letters*, 388, 138307.
- Zoey (2018). WinSun print into the future. https://digital.hbs.edu/platform-rctom/submission/winsun-print-into-the-future/ [accessed 27-08-2025].